AIAA JOURNAL
Vol. 33, No. 7, July 1995

High-Order Hybrid Numerical Simulations of Two-Dimensional Detonation Waves

Wei Cai*
University of North Carolina at Charlotte, Charlotte, North Carolina 28223

To study multidimensional unstable detonation waves, we have developed a high-order numerical scheme suitable for calculating the detailed transverse wave structures of multidimensional detonation waves. The numerical algorithm uses a multidomain approach so that different numerical techniques can be applied for different components of detonation waves. The detonation waves are assumed to undergo an irreversible, unimolecular reaction $A \rightarrow B$. Several cases of unstable two-dimensional detonation waves are simulated, and detailed transverse wave interactions are documented. The numerical results show the importance of resolving the detonation front without excessive numerical viscosity to obtain the correct cellular patterns.

Nomenclature

A = reactant
$\boldsymbol{A}$ = Jacobian matrix, $\partial \boldsymbol{F}/\partial \boldsymbol{U}$
a = local sound speed
a_0 = local sound speed in unreacted gas
B = product
$\boldsymbol{B}$ = Jacobian matrix, $\partial \boldsymbol{G}/\partial \boldsymbol{U}$
C = cross point between subdomains
D = detonation speed
D_j = $C - J$ speed of steady detonation waves
E^+ = activation energy
e = specific internal energy
$\boldsymbol{F}$ = ξ flux in curvilinear (ξ, η) coordinates
f = overdrive of Chapman-Jouguet detonation waves
f^* = critical overdrive of steady detonation waves
$\boldsymbol{f}$ = x flux in (x, y) coordinates
$\boldsymbol{G}$ = η flux in curvilinear(ξ, η)coordinates
$\boldsymbol{g}$ = y flux in (x, y) coordinates
$\sqrt{g}$ = Jacobian matrix of mesh transformation
K = constant
l_i = left eigenvalues of $\boldsymbol{A}$ or $\boldsymbol{B}$
l^* = half-reaction distance
lsk = mesh size for detonation front
M_i = molecular weight of ith species
$\boldsymbol{n}$ = normal direction of shock front
(n, m) = mesh size in (ξ, η) direction, respectively
p = pressure
Q = specific heat formation
$\boldsymbol{r}_i$ = right eigenvalues of $\boldsymbol{A}$ or $\boldsymbol{B}$
s = entropy
T = temperature
$\boldsymbol{T}$ = $\partial \boldsymbol{v}/\partial \boldsymbol{u}$
t = time
$\boldsymbol{t}$ = tangential direction of shock front
t^* = half-reaction time
$\boldsymbol{U}$ = conservative variables in curvilinear (ξ, η) coordinates
U^1 = contravariant velocity, $\xi_t + u\xi_x + v\xi_y$
U^2 = contravariant velocity, $\eta_t + u\eta_x + v\eta_y$
u = flow x velocity
$\boldsymbol{u}$ = conservative variables in (x, y) coordinates
v = flow y velocity
$\boldsymbol{v}$ = primitive variables in (x, y) coordinates
W = channel width
(x, y) = spatial coordinates
γ = ratio of specific heats
λ_i = mass fraction of ith species
μ_{ij} = stoichiometric coefficients for jth species in ith reaction step
(ξ, η) = curvilinear spatial coordinates
$\Pi_3(x)$ = cubic Hermite interpolation polynomial
ρ = density
ρ_i = density of ith species
Φ = right-hand side
Ψ = right-hand side
ω_i = reactant rate of ith reaction step

Received Aug. 4, 1993; revision received Aug. 22, 1994; accepted for publication Oct. 4, 1994.

*Associate Professor, Department of Mathematics; currently Associate Professor, Department of Mathematics, University of California, Santa Barbara, CA 93106.

I. Introduction

DETONATION waves are intrinsically multidimensional unstable phenomenon as demonstrated by the experiments of Urtiew and Oppenheim.[1] Since then, the simple steady Chapman–Jouquet theory[2,3] has been re-examined for its limited explanation of most of the multidimensional features seen in real-world detonation waves. The unique characteristics of multidimensional detonation waves are their cellular patterns that are the trajectories recorded on the wall by the transverse waves structures. Those transverse wave structures consist of so-called "triple points" that have three shock configurations[4] (an incident shock, a reflected shock, and a Mach stem plus a contact discontinuity). The formation of those transverse wave structures moving along the main precursor detonation front attracted much attention. These phenomena raised the interest of experimentalists trying to measure the cell size of the cellular pattern.[5]

In this paper, we will present a high-order hybrid method to study two-dimensional detonation waves. The numerical simulations done in the paper are for an idealized model of a chemical reaction in which the reactant species is in an irreversible, unimolecular reaction $A \rightarrow B$ with finite Arrhenius reaction rate. It is evident that this model cannot represent all of the effects of realistic chemical kinetics on the cellular structures observed in lab experiments. However, an accurate numerical solution of this simplified model will provide a better understanding of the physics involved in the onset and evolution of detonation waves.

There are three basic characteristics of detonation waves: 1) a strong precursor detonation front, 2) Mach stem configuration of the "triple points" and transverse wave structures, and 3) stiff chemical reactions. The flowfield can be divided into regions of highly irregular and steep gradients near the detonation front and regions of strong but smooth pressure waves. Near the shock fronts, strong vorticity fields are generated from the roll-up of slip lines. The temporal changes of thermodynamic and chemical compositions vary dramatically from region to region. We will construct our hybrid numerical schemes according to these characteristics of multidimensional detonation waves.

The reaction rate depends on the flow temperature exponentially through the Arrhenius relation. Accurate computations of the

flowfield are extremely important in producing the correct chemical reactions and thus the correct cellular structures. Traditional shock-capturing schemes, designed to smooth shock and contact discontinuities, introduce a considerable amount of numerical viscosity near those discontinuities. They have been shown to have a tendency to distort the real chemical reaction processes. In Ref. 6, the widely used PPM high-order Godunov scheme was found to produce nonphysical weak detonations. Also in Ref. 7, the ENO finite difference scheme was shown to yield wrong detonation speeds in one-dimensional ZND simulations. All of these facts point out the importance of designing numerical methods without excessive numerical viscosity.

In Sec. II, we will introduce the governing equations for reacting flows and their formulation in general curvilinear coordinates. In Sec. III, we discuss the hybrid numerical scheme. In Sec. IV, we consider the treatment of interface conditions between different numerical schemes and the smoothing techniques for the detonation front. We validate the hybrid numerical scheme and test the effects of smoothing of the detonation front on the cellular pattern of detonation waves. Then, we present simulations of two cases of two dimensional detonation waves. In Sec. V a conclusion is given.

II. Governing Equations

Consider two-dimensional detonation waves in an infinite channel moving from left to right into unreacted gas mixtures where the channel is denoted by $\Omega = (-\infty, \infty) \times [-W/2, W/2]$ where W is the channel width. The governing equations for reacting detonation waves with s species and p reaction steps are the following Euler equations:

$$\frac{\partial \boldsymbol{u}}{\partial t} + \frac{\partial \boldsymbol{f}(\boldsymbol{u})}{\partial x} + \frac{\partial \boldsymbol{g}(\boldsymbol{u})}{\partial y} = \Phi(\boldsymbol{u}) \tag{1}$$

where

$$\boldsymbol{u} = (\rho, \rho u, \rho v, \rho e, \rho_1, \ldots, \rho_s)^{\top}$$

$$\boldsymbol{f}(\boldsymbol{u}) = \left[\rho u, \rho u^2 + p, \rho uv, \rho u\left(e + \frac{p}{\rho}\right), \rho_1 u, \ldots, \rho_s u\right]^{\top}$$

$$\boldsymbol{g}(\boldsymbol{u}) = \left[\rho v, \rho vu, \rho v^2 + p, \rho v\left(e + \frac{p}{\rho}\right), \rho_1 v, \ldots, \rho_s v\right]^{\top}$$

$$\Phi(\boldsymbol{u}) = (0, 0, 0, 0, \omega_1, \ldots, \omega_s)^{\top}$$

and $\omega_i = \rho M_i \sum_{i=1}^{p} \nu_{ij} (\partial \lambda_i / \partial t)$, and $(\mathrm{d}\lambda_i/\mathrm{d}t)$ denotes the change rate of the ith reaction progress variable, which is assumed to obey Arrhenius' rule. In the case of one-step $A \rightarrow B$ irreversible reaction, i.e., $s = p = 1$ and

$$\omega = -\boldsymbol{K}\rho\lambda e^{-E^+/T} \tag{2}$$

where $\lambda = \rho_1/\rho$ is the mass fraction of the reactant. If we assume exothermic reaction, the specific internal energy

$$e = \frac{p}{(\gamma - 1)\rho} + \frac{u^2 + v^2}{2} + \lambda Q \tag{3}$$

where Q is the specific heat formation and $\gamma = 1.2$ is the ratio of specific heats.

All previous quantities have been nondimensionalized by the initial states in the unreacted gas mixture in front of the detonation fronts. They are given as follows ($\leftarrow$ indicates nondimensionalization and the subscript 0 denotes states of unreacted gas)

$$p \leftarrow \frac{p}{p_0}$$

$$\rho \leftarrow \frac{\rho}{\rho_0}$$

$$\boldsymbol{u} \leftarrow \frac{\boldsymbol{u}}{\sqrt{RT_0}}$$

$$T \leftarrow \frac{T}{T_0}$$

$$E^+ \leftarrow \frac{E^+}{RT_0}$$

$$Q \leftarrow \frac{Q}{RT_0}$$

$$t \leftarrow \frac{t}{t^*}$$

$$x \leftarrow \frac{x}{l^*}$$

where $t^* = (l^*/\sqrt{RT_0})$, ℓ^* is the half-reaction distance that a mass particle will travel from the detonation front before half-depletion of the reactant occurs.

Consider general curvilinear coordinates (ξ, η, t), $\xi = \xi(x, y, t)$, $\eta = \eta(x, y, t)$; the governing equation (1) becomes

$$\frac{\partial \boldsymbol{U}}{\partial t} + \frac{\partial \boldsymbol{F}(\boldsymbol{U})}{\partial \xi} + \frac{\partial \boldsymbol{G}(\boldsymbol{U})}{\partial \eta} = \Psi(\boldsymbol{U}) \tag{4}$$

where $\boldsymbol{U} = \sqrt{g}\boldsymbol{u}$,

$$\boldsymbol{F}(\boldsymbol{U}) = \begin{bmatrix} U^1\sqrt{g}\rho \\ U^1\sqrt{g}\rho u + y_\eta p \\ U^1\sqrt{g}\rho v - x_\eta p \\ U^1\sqrt{g}\rho e + (y_\eta u - x_\eta v)p \\ U^1\sqrt{g}\rho_1 \\ \vdots \\ U^1\sqrt{g}\rho_s \end{bmatrix}$$

$$\boldsymbol{G}(\boldsymbol{U}) = \begin{bmatrix} U^2\sqrt{g}\rho \\ U^2\sqrt{g}\rho u - y_\xi p \\ U^2\sqrt{g}\rho v + x_\xi p \\ U^2\sqrt{g}\rho e + (-y_\xi u + x_\xi v)p \\ U^2\sqrt{g}\rho_1 \\ \vdots \\ U^2\sqrt{g}\rho_s \end{bmatrix} \tag{5}$$

$$\Psi(\boldsymbol{U}) = \left(0, 0, 0, 0, \sqrt{g}\omega_1, \ldots, \sqrt{g}\omega_s\right)^{\top}$$

where $\sqrt{g} = x_\xi y_\eta - x_\eta y_\xi$ is the Jacobian of the mesh transformation, $U^1 = \xi_t + u\xi_x + v\xi_y$, and $U^2 = \eta_t + u\eta_x + v\eta_y$. The spatial discretization is done in the (ξ, η) space for Eq. (4), and the range for ξ, η are both $[-1, 1]$.

III. Hybrid Numerical Algorithm

The computational region consists of the detonation front moving to the right and the rear piston boundary and upper and lower solid walls. It will be subdivided using the multidomain technique with the detonation front as the right most boundary (see Fig. 1). Three different numerical techniques will be applied in different parts of the computational region. They are a shock-tracking algorithm for the detonation front, a high-order ENO finite difference scheme in the subdomain that contains the reflected shocks and contact discontinuities along the detonation front, and the Chebyshev collocation methods for the strong vorticity and pressure fields from the interaction of transverse waves along the detonation front. We refer the reader to Ref. 8 for the details of this method. The reason for using Chebyshev collocation methods is because of their higher accuracy and efficiency for the same number of mesh points than a shock-capturing scheme such as the ENO schemes; a detailed CPU performance comparison between these two methods can been found in Ref. 9.

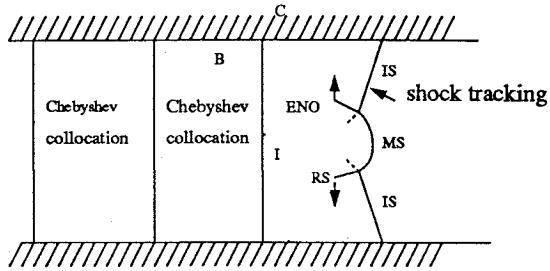

Fig. 1 Multidomain setup for the hybrid numerical scheme for detonation waves.

We give brief descriptions of the ENO finite difference method and the shock-tracking scheme used in our algorithm.

High-Order ENO Finite Difference Methods

To apply the ENO finite difference method to Eq. (4), the spatial derivative is discretized by conservative numerical flux differences:

$$\frac{\partial U_{i,j}}{\partial t}+\frac{\hat{F}_{i+\frac{1}{2},j}-\hat{F}_{i-\frac{1}{2},j}}{\Delta\xi}+\frac{\hat{G}_{i,j+\frac{1}{2}}-\hat{G}_{i,j-\frac{1}{2}}}{\Delta\eta}=\Psi(U_{i,j}) \tag{6}$$

where $U_{i,j}$ is the numerical approximation of Eq. (4) using the method of lines. To compute the numerical fluxes $\hat{F}_{i+\frac{1}{2},j}$, and $\hat{G}_{i,j+\frac{1}{2}}$, first the primitive functions for $\boldsymbol{F}$ and $\boldsymbol{G}$ are approximated by piecewise polynomials using the ENO adaptive stencil idea of Harten,[10] and then the derivatives of those polynomials are evaluated at the edge-centered mesh points $(\xi_{i+\frac{1}{2}}, \eta_j)$ and $(\xi_i, \eta_{j+\frac{1}{2}})$ to produce the numerical fluxes. For technical details on the construction of ENO fluxes to the system of equations (4), we refer the reader to Refs. 10 and 11.

We need the eigenvalues and eigenvector on the Jacobian of fluxes $\boldsymbol{A}=\partial\boldsymbol{F}/\partial\boldsymbol{U}$ and $\boldsymbol{B}=\partial\boldsymbol{G}/\partial\boldsymbol{U}$ for the characteristic decompositions to define the ENO fluxes. If $(\mathrm{D}/\mathrm{D}t)=(\partial/\partial t)+u(\partial/\partial x)+v(\partial/\partial y)$ denotes the material derivative, then the eigenvalues of $\boldsymbol{A}$ are $(\mathrm{D}\xi/\mathrm{D}t)-\sqrt{\xi_x^2+\xi_y^2}a$, $(\mathrm{D}\xi/\mathrm{D}t)$, $(\mathrm{D}\xi/\mathrm{D}t)$, $(\mathrm{D}\xi/\mathrm{D}t)$, $(\mathrm{D}\xi/\mathrm{D}t)+\sqrt{\xi_x^2+\xi_y^2}a$, and those of $\boldsymbol{B}$ are $(\mathrm{D}\eta/\mathrm{D}t)-\sqrt{\eta_x^2+\eta_y^2}a$, $(\mathrm{D}\eta/\mathrm{D}t)$, $(\mathrm{D}\eta/\mathrm{D}t)$, $(\mathrm{D}\eta/\mathrm{D}t)$, $(\mathrm{D}\eta/\mathrm{D}t)+\sqrt{\eta_x^2+\eta_y^2}a$. The corresponding five left and right eigenvectors are $\boldsymbol{l}_i\boldsymbol{T}$, $\boldsymbol{T}^{-1}\boldsymbol{r}_i$, $i=1,\ldots,5$, respectively, and

$$\begin{aligned}
&\boldsymbol{l}_1=(1,-\alpha\rho a,-\beta\rho a,0,0) && \boldsymbol{r}_1=\frac{1}{2}\left(1,-\frac{\alpha}{\rho a},-\frac{\beta}{\rho a},\frac{1}{a^2},0\right)^{\mathsf{T}}\\
&\boldsymbol{l}_2=(0,-\beta,\alpha,0,0) && \boldsymbol{r}_2=(0,-\beta,\alpha,0,0)^{\mathsf{T}}\\
&\boldsymbol{l}_3=(1,0,0,-a^2,0) && \boldsymbol{r}_3=\left(0,0,0,-\frac{1}{a^2},0\right)^{\mathsf{T}}\\
&\boldsymbol{l}_4=(0,0,0,0,1) && \boldsymbol{r}_4=(0,0,0,0,1)^{\mathsf{T}}\\
&\boldsymbol{l}_5=(1,\alpha\rho a,\beta\rho a,0,0) && \boldsymbol{r}_5=\frac{1}{2}\left(1,\frac{\alpha}{\rho a},\frac{\beta}{\rho a},\frac{1}{a^2},0\right)^{\mathsf{T}}
\end{aligned} \tag{7}$$

where $a=\sqrt{\gamma p/\rho}$ is the sound speed and $\alpha=\xi_x/\sqrt{\xi_x^2+\xi_y^2}$, $\beta=\xi_y/\sqrt{\xi_x^2+\xi_y^2}$ for $\boldsymbol{A}$ and $\alpha=\eta_x/\sqrt{\eta_x^2+\eta_y^2}$, $\beta=\eta_y/\sqrt{\eta_x^2+\eta_y^2}$ and the transform matrix $\boldsymbol{T}=\partial\boldsymbol{v}/\partial\boldsymbol{u}$ with $\boldsymbol{v}=(p,u,v,\rho,\lambda)$ being the primitive variables,

$$\boldsymbol{T}=\begin{bmatrix}
\frac{\gamma-1}{2}(u^2+v^2) & -(\gamma-1)u & -(\gamma-1)v & (\gamma-1) & -(\gamma-1)Q\\
-\frac{u}{\rho} & \frac{1}{\rho} & 0 & 0 & 0\\
-\frac{v}{\rho} & 0 & \frac{1}{\rho} & 0 & 0\\
1 & 0 & 0 & 0 & 0\\
\frac{\lambda}{\rho} & 0 & 0 & 0 & \frac{1}{\rho}
\end{bmatrix} \tag{8}$$

Tracking Algorithm for Precursor Detonation Front

The detonation front will be represented by a continuous curve

$$x=x(y,t),\qquad \frac{-W}{2}\le y\le\frac{W}{2},\qquad t\ge 0 \tag{9}$$

and the normal of the front denoted by $\boldsymbol{n}=(n_x,n_y)$ points to the unreacted gas, which can be computed by

$$\begin{aligned}
n_x&=\frac{1}{\sqrt{1+(x_y)^2}}\\
n_y&=\frac{-x_y}{\sqrt{1+(x_y)^2}}
\end{aligned} \tag{10}$$

By Huygen's principle, the detonation front will propagate in its normal direction with speed

$$D_n=\frac{x_t}{\sqrt{1+(x_y)^2}} \tag{11}$$

Following the procedure proposed in Ref. 12, we can write the Rankine–Hugoniot condition across the shock front as follows:

$$\begin{cases}
\rho_0(u_{n,0}-D_n)=\rho_1(u_{n,1}-D_n)\\
\rho_0(u_{n,0}-D_n)^2+p_0=\rho_1(u_{n,1}-D_n)^2+p_1\\
\dfrac{\gamma}{\gamma-1}\dfrac{p_0}{\rho_0}+\frac{1}{2}(u_{n,0}-D_n)^2+\lambda_0 Q=\dfrac{\gamma}{\gamma-1}\dfrac{p_1}{\rho_1}\\
\qquad+\frac{1}{2}(u_{n,1}-D_n)^2+\lambda_1 Q\\
\rho_0\lambda_0(u_{n,0}-D_n)=\rho_1\lambda_1(u_{n,1}-D_n)
\end{cases} \tag{12}$$

where 0 denotes the state in front of the detonation front and 1 the states behind the front. And $u_n=(u,v)\circ\boldsymbol{n}$ is the normal velocity on the front. Equation (12) relates the states in front of the shock and behind the shock. To close the system, we need to impose the continuity of tangential velocity, i.e.,

$$u_{t,0}=u_{t,1} \tag{13}$$

where $u_t=(-n_y,n_x)\circ(u,v)$ is the tangential velocity.

From Eqs. (12) and (13), we can solve the quantities $(p_1,\rho_1,u_{n,1},u_{t,1},\lambda_1)$ behind the shock in terms of those in front of the shock $(p_0,\rho_0,u_{n,0},u_{t,0},\lambda_0)$. Using the notation in Ref. 13, we have the following,

$$\begin{aligned}
\rho_1&=\rho_0\frac{(\gamma+1)\kappa^2}{(\gamma\kappa^2+1)(1-w)}\\
p_1&=p_0\frac{(\gamma\kappa^2+1)(1+w\gamma)}{\gamma+1}\\
u_{n,1}&=u_{n,0}-(u_{n,0}-D_n)\left(1-\frac{\rho_0}{\rho_1}\right)\\
u_{t,1}&=u_{t,0}\\
\lambda_1&=\lambda_0
\end{aligned} \tag{14}$$

where $w=(\kappa^2-1)/(\gamma\kappa^2+1)$, $\kappa=|D_n-u_{n,0}|a_0$ is the Mach number of the shock front relative to the unreacted gas, and $a_0=\sqrt{\gamma p_0/\rho_0}=\sqrt{\gamma}$ is the sound speed in the unreacted mixture.

To derive a time evolution equation for the shock front, we define the time differentiation along the shock front $\mathrm{d}/\mathrm{d}t = \partial/\partial t + x_t(y,t)\partial/\partial x$ for any fixed $y \in [-W/2, W/2]$. By applying $\mathrm{d}/\mathrm{d}t$ on both sides of Eq. (14) and separating the terms that involve $x_{tt}(y,t)$, we obtain the following,

$$\begin{aligned}
\frac{\mathrm{d}p_1}{\mathrm{d}t} &= c_1 x_{tt} + d_1 \\
\frac{\mathrm{d}\rho_1}{\mathrm{d}t} &= c_2 x_{tt} + d_2 \\
\frac{\mathrm{d}u_1}{\mathrm{d}t} &= c_{3,u} x_{tt} + d_{3,u} \\
\frac{\mathrm{d}v_1}{\mathrm{d}t} &= c_{3,v} x_{tt} + d_{3,v} \\
\frac{\mathrm{d}\lambda_1}{\mathrm{d}t} &= c_4 x_{tt} + d_4
\end{aligned} \tag{15}$$

where

$$c_1 = \frac{4\rho_0\tau}{(1+\gamma)\left[1+(x_y)^2\right]}$$

$$d_1 = \frac{\mathrm{d}p_0}{\mathrm{d}t}\frac{2\gamma\kappa^2+1-\gamma}{1+\gamma} - \frac{2\rho_0}{(1+\gamma)\left[1+(x_y)^2\right]}\left[2\tau N_t + \kappa^2 S_t\right]$$

$$c_2 = \frac{4(\gamma+1)\kappa^2}{\tau[(\gamma-1)\kappa^2+2]^2}$$

$$d_2 = \frac{\rho_1}{\rho_0}\frac{\mathrm{d}\rho_0}{\mathrm{d}t} + \frac{2(\gamma+1)\rho_0\kappa^2}{[(\gamma-1)\kappa^2+2]^2}\left(\frac{2N_t}{\tau} - \frac{S_t}{S}\right)$$

$$c_{3,u} = \frac{c_{3,n} + x_y c_{3,t}}{1+(x_y)^2}$$

$$d_{3,u} = \frac{d_{3,n} + x_y d_{3,t}}{1+(x_y)^2}$$

$$c_{3,v} = \frac{-x_y c_{3,n} + c_{3,t}}{1+(x_y)^2}$$

$$d_{3,v} = \frac{-x_y d_{3,n} + d_{3,t}}{1+(x_y)^2}$$

$$c_{3,n} = \frac{2}{\gamma+1}\left(1+\frac{1}{\kappa^2}\right), \qquad c_{3,t} = 0$$

$$d_{3,n} = x_{yt}v_1 + \frac{(\gamma-1)\kappa^2-2}{(\gamma+1)\kappa^2}N_t - \frac{2}{(\gamma+1)}\frac{S_t}{\tau}$$

$$g_{3,t} = P_t - x_{yt}u_1$$

$$f_4 = 0, \qquad g_4 = \frac{\mathrm{d}\lambda_0}{\mathrm{d}t}$$

and $S = [1+(x_y)^2]a_0^2$, $N = u_0 - x_y v_0$, $P = x_y u_0 + v_0$, $N_t = \mathrm{d}N/\mathrm{d}t$, $\tau = x_t - u_0 + x_y v_0$, $P_t = \mathrm{d}P/\mathrm{d}t$, and $S_t = \mathrm{d}S/\mathrm{d}t$.

Using $\mathrm{d}\boldsymbol{v}_1/\mathrm{d}t = (\partial \boldsymbol{v}/\partial \boldsymbol{u})(\mathrm{d}\boldsymbol{u}_1/\mathrm{d}t) = \boldsymbol{T}(\mathrm{d}\boldsymbol{u}_1/\mathrm{d}t)$, Eq. (15) can be rewritten for conservative variable $\boldsymbol{u}$,

$$\boldsymbol{T}\frac{\mathrm{d}\boldsymbol{u}_1}{\mathrm{d}t} = \boldsymbol{T}\boldsymbol{c}x_{tt} + \boldsymbol{T}\boldsymbol{d} \tag{16}$$

where $\boldsymbol{c} = (c_1, c_2, c_{3,u}, c_{3,v}, c_4)^\top$ and $\boldsymbol{d} = (d_1, d_2, d_{3,u}, d_{3,v}, d_4)^\top$.

Now on a fixed point on the shock front we consider the characteristic component of Eq. (1) in the normal direction $\boldsymbol{n} = [1/\sqrt{1+(x_y)^2}, -x_y/\sqrt{1+(x_y)^2}]$,

$$\frac{\partial \boldsymbol{u}}{\partial t} + \frac{\partial}{\partial \boldsymbol{n}}\tilde{\boldsymbol{f}} + \frac{\partial}{\partial \boldsymbol{t}}\tilde{\boldsymbol{g}} = \Phi \tag{17}$$

where $\tilde{\boldsymbol{f}} = n_x\boldsymbol{f} + n_y\boldsymbol{g}$ and $\tilde{\boldsymbol{g}} = -n_y\boldsymbol{f} + n_x\boldsymbol{g}$. The eigenvalues and eigenvector of Jacobian matrix $\tilde{\boldsymbol{A}} = \partial\tilde{\boldsymbol{f}}/\partial\boldsymbol{u}$ are

$$u_n - c,\ u_n,\ u_n,\ u_n,\ u_n + c \tag{18}$$

$$\boldsymbol{l}_1\boldsymbol{T}, \boldsymbol{l}_2\boldsymbol{T}, \ldots, \boldsymbol{l}_5\boldsymbol{T} \tag{19}$$

where $\boldsymbol{l}_i$, $i = 1, \ldots, 5$ are given in Eq. (7) with $\alpha = 1/\sqrt{1+(x_y)^2}$, $\beta = -x_y/\sqrt{1+(x_y)^2}$, and $u_n = \alpha u + \beta v$.

Along the normal direction of the shock front, the $(u_n + c)$-characteristic field approaches the shock front from behind; therefore a compatibility condition can be obtained by considering the characteristic combination of Eq. (16)

$$\boldsymbol{l}_5\boldsymbol{T}\frac{\mathrm{d}\boldsymbol{u}_1}{\mathrm{d}t} = \boldsymbol{l}_5\boldsymbol{T}\boldsymbol{c}x_{tt} + \boldsymbol{l}_5\boldsymbol{T}\boldsymbol{d} \tag{20}$$

thus yielding the following ODE for the shock speed

$$x_{tt} = H(\boldsymbol{u}_1, \boldsymbol{u}_0, x_y, x_t, x_{ty}) \tag{21}$$

where

$$H = \left(\boldsymbol{l}_5\boldsymbol{T}\frac{\mathrm{d}\boldsymbol{u}_1}{\mathrm{d}t} - \boldsymbol{l}_5\boldsymbol{T}\boldsymbol{d}\right)\Big/\boldsymbol{l}_5\boldsymbol{T}\boldsymbol{c}$$

and

$$\frac{\mathrm{d}\boldsymbol{u}_1}{\mathrm{d}t} = \boldsymbol{U}_1\frac{\mathrm{d}}{\mathrm{d}t}\frac{1}{\sqrt{\boldsymbol{g}}} + \frac{1}{\sqrt{\boldsymbol{g}}}\frac{\partial \boldsymbol{U}_1}{\partial t}$$

and $\partial \boldsymbol{U}_1/\partial t = -\partial \boldsymbol{F}(\boldsymbol{U})/\partial\xi - \partial \boldsymbol{G}(\boldsymbol{U})/\partial\eta + \Psi(\boldsymbol{U})$ is the residual computed in (ξ, η) space behind the shock front.

Interface Conditions

A correct interface coupling between subdomains is crucial for the global stability and accuracy of the scheme. The basic idea behind the treatment of interface and boundary condition is the propagation of information along characteristics of the hyperbolic systems.[14] Let us consider the cross points between the wall boundary and interior interface—"C" points (Fig. 1).

To update the solution for point "C" we have to consider the information that comes from both subdomains Ω_l and Ω_r and also the role of the wall. Characteristic surfaces approaching the point "C" from several direction can be used to form a closed system to determine this solution.[14]

First let us consider the characteristic surface that is tangential to the interface Γ with normal $\boldsymbol{n} = (1, 0)$. The corrected characteristic quantities w_1, w_4, and w_5 can be obtained as follows: assuming λ_1, λ_4, and λ_5 are all positive (otherwise, replace subscript "l" by "r" for each negative values of $\lambda_i - S_{\Gamma,C}$, $i = 1, 4, 5$),

$$w_1^x = w_1^{\text{corrected}} = p^l - \bar{a}\bar{\rho}u_n^l \tag{22}$$

$$w_4^x = w_4^{\text{corrected}} = \lambda^l \tag{23}$$

$$w_5^x = w_5^{\text{corrected}} = p^l + \bar{a}\bar{\rho}u_n^l. \tag{24}$$

where subscript x indicates the normal direction of the characteristic surface and $u_n = \boldsymbol{u} \circ \boldsymbol{n}$.

On the other hand, we know that the entropy s remains constant along the characteristic direction corresponding to the eigenvalue $u_n = \boldsymbol{u} \circ \boldsymbol{n}$, and we can correct the entropy s as follows:

$$s^{\text{corrected}} = \begin{cases} \dfrac{p^l}{(\rho^l)^\gamma} & \text{if} \quad u_n - S_{\Gamma,C} > 0 \\ \dfrac{p^r}{(\rho^r)^\gamma} & \text{otherwise} \end{cases} \tag{25}$$

Next, we consider the characteristic surface approaching the wall at point "C" with normal $\boldsymbol{n} = (0, 1)$ (top wall) or $(0, -1)$ (lower wall). On the top wall, $u_n = v = 0$, and so $\lambda_l = u_n - a = -a$, and we have the first characteristic field approaching the wall from the computational domain. Therefore, we can correct the first

characteristic variable w_1^y using the results from either Ω_l or Ω_r, i.e.,

$$w_1^y = w_1^{\text{corrected}} = \begin{cases} p^l + \bar{a}\bar{\rho}u_n^l & \text{if } u_n - S_{\Gamma,C} > 0 \\ p^r + \bar{a}\bar{\rho}u_n^r & \text{otherwise} \end{cases} \tag{26}$$

Finally, we solve for all four primitive quantities of the flow as follows:

$$v = 0 \tag{27}$$

$$\lambda = w_4 \tag{28}$$

$$p = \left(w_1^x + w_5^x + 2w_1^y\right)/4 \tag{29}$$

$$\rho = \left(\frac{p}{s}\right)^{\frac{1}{\gamma}} \tag{30}$$

The treatment of the cross point on the lower wall can be done similarly.

Smoothing Technique of Detonation Front

To evolve the detonation front, we need to compute the time derivative of its normal speed D_n, which depends on x_{tt}. Thus, the accuracy of the detonation front depends on the residual of the numerical solution at the detonation front. Numerical experiments show that the front will develop high-frequency numerical instability if no smoothing is applied on the detonation front. In this paper, we test three types of smoothing on the detonation front and compare the effects of different smoothings on the cellular pattern of detonation waves.

Smoothing I—Averaging Solution on the Detonation Front

In Eq. (21) we replace $\boldsymbol{u}_{1,j}$ by the simple average of neighboring solutions,

$$\boldsymbol{u}_{1,j} \longleftarrow \frac{\boldsymbol{u}_{1,j-1} + 2\boldsymbol{u}_{1,j} + \boldsymbol{u}_{1,j+1}}{4} \tag{31}$$

It can be seen that this averaging procedure will reduce the accuracy of the shock front to only first order and have a larger dissipation than the other smoothing techniques suggested later.

Smoothing II—Derivative Smoothing

Let $(x_i, y_i), i = 1, \ldots, n$, be n discrete data points and $x_1 < x_2 \cdots < x_n$. The cubic Hermite interpolation $\Pi_3(x)$ is a piecewise cubic polynomial that has a continuous derivative at nodes x_i and satisfies the following conditions,

$$\begin{cases} \Pi_3(x_i) = y_i \\ \Pi_3'(x_i) = y_i' \end{cases} \qquad 1 \le i \le n \tag{32}$$

and

$$y_i' = \frac{\Delta_{i-1}s_i + \Delta_{i-1}s_{i-1}}{\Delta_{i-1} + \Delta x_i} \qquad 2 \le i \le n-1$$

where $s_i = (y_{i+1} - y_i)/\Delta x_i$ and $\Delta x_i = x_{i+1} - x_i$. The derivative at the endpoints is given by appropriate one-sided differences.

To maintain the monotonicity of the original data, we limit the derivatives y_i',[15]

$$y_i' \longleftarrow y_{\text{lim},i}' = \begin{cases} \min[\max(0, y_i'), 3\min(s_{i-1}, s_i)] & \text{if } y_i' > 0 \\ \max[\min(0, y_i'), -3\min(s_{i-1}, s_i)] & \text{if } y_i' \le 0 \end{cases} \tag{33}$$

Then we change x_y' in H of Eq. (21) as follows,

$$(x_y')_i \longleftarrow (x_y')_{\text{lim},i}, \qquad 1 \le i \le n \tag{34}$$

Smoothing Technique III—High-Frequency Spectral Space Smoothing

The third smoothing technique applies high-frequency cutoff functions in the Fourier transform space of the detonation front. Assume that the discrete data x_i, $1 \le i \le n$, are equally distributed and data (x_i, y_i) are decomposed into Fourier modes,

$$y_i = \sum_{k=-\frac{n}{2}}^{\frac{n}{2}-1} \hat{y}_k e^{ikx_i} \qquad 1 \le i \le n \tag{35}$$

where $\hat{y}_k = (1/n)\sum_{i=1}^{n} y_i e^{-ikx_i}$.

We multiply the Fourier coefficient $\hat{y}_k$ by a decreasing factor σ_k so that the high frequencies will be decreased. The modified y_i is given by

$$y_i \leftarrow (y_i)^{\text{filtered}} =: \sum_{k=-\frac{n}{2}}^{\frac{n}{2}-1} \sigma_k \hat{y}_k e^{ikx_i} \qquad 1 \le i \le n \tag{36}$$

Here we chose σ_k so that it decays exponentially in terms of the wave number,

$$\sigma_k = e^{-\mu\left(\frac{2k}{n}\right)^{2l}} \qquad \text{for } |k| \le \frac{n}{2} \tag{37}$$

where the constant μ is chosen so that $\sigma_{n/2}$ is the machine zero and $2l(l = 6)$ is called the order of the exponential filtering.

IV. Numerical Results

Recently, the numerical studies of two-dimensional detonation waves have received renewed interest since the early results by Taki and Fujiwara[16] and Oran et al.[17] Especially, the simulations done by Bourlioux and Majda[18] with an improved PPM scheme and those by Quirk[19] with a sophisticated adaptive Godunov-type scheme have improved the state of the art of detonation wave simulations.

Our computation starts with the ZND steady-state solution of a plane detonation wave. To induce the transverse waves, we introduce perturbations either in the detonation front or in the flow variables themselves, or both. The type of perturbations used will be sinelike wave

$$x(y, 0) =: x(y, 0) + \epsilon \sin(\pi y^2), \qquad -W/2 \le y \le W/2 \tag{38}$$

or random perturbations [$\epsilon \text{ran} f()$]. Solid boundary conditions will be used in all computations.

To predict the cell size of detonation waves with a simple one-step reaction as in this paper, Erpenbeck studied the linearized Euler system and based the cell size on the most unstable mode under multidimensional disturbances.[20] Another approach consists of the work of Strehlow et al.[21] and, more recently, that of Majda[22]; both used the idea of ray trapping of acoustic waves near a steady detonation front. In Ref. 22, an explicit time-dependent amplifying mechanism and nonlinearity for small-amplitude high-frequency waves were also considered in deriving the criteria of transverse wave formation and cell size. However, as far as comparison with the simulations done in this paper is concerned, these theoretical results cannot be applied directly. In the linear mode analysis of Erpenbeck, a periodic boundary condition is assumed in the transverse direction; thus the effect of a channel wall boundary on the cellular pattern cannot be accounted for. Also, in the acoustic ray trapping approaches of Strehlow et al.[21] and Majda,[22] the solid wall effect is also ignored. In Ref. 18, a numerical verification of the proposed acoustic ray trapping theory gives very incidental agreement. The reason for such disagreement could be that both linear mode analysis and high-frequency asymptotic with acoustic ray trapping are done assuming that the amplitude of perturbations are small and nonlinear effects can be ignored. However, in most of the numerical computations, large amplitude nonlinear effects could be the deciding effects on the cellular pattern.

Meanwhile, the experimental data on cell size of oxygen and hydrogen[21] and other fuels (methane, acetylene, or ethylene)[23] demand much more complicated chemical kinetics such as the one-step reaction that can be handled by our algorithm in this paper. Therefore, at this time we were unable to present any quantitative

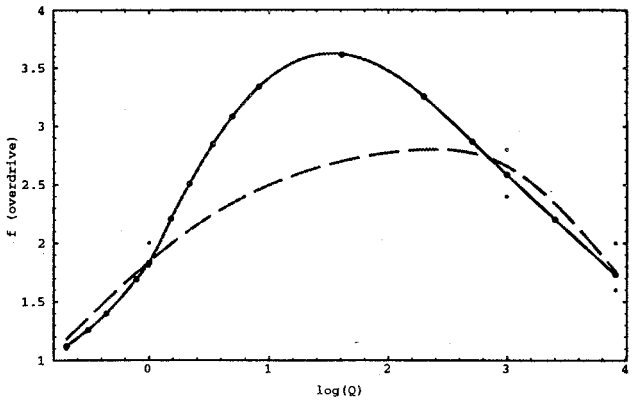

Fig. 2 Neutral stability curve of one-dimensional ZND detonation waves.

comparison results with either theoretical results or experimental data.

Validation of Numerical Scheme

Calculation Results of Neutral Stability Curve of One-Dimensional Detonation Waves

To validate our hybrid scheme, we have calculated the neutral stability curve of one-dimensional detonation waves in the presence of one-dimensional disturbances as studied in Ref. 13. For one dimensional detonation waves with a one-step irreversible reaction, for a given heat formation Q, the overdrive parameter f, defined by $f = (D/D_j)^2$ with D_j being the Chapman–Jouguet detonation speed, determines its stability. There is a critical overdrive f^* such that the steady one-dimensional detonation wave will be stable if $f > f^*$ and unstable if $f < f^*$ under one-dimensional perturbations. For $Q = 50$ and $E^+ = 50$, Erpenbeck predicted $f^* = 1.76$.[13]

In Fig. 2, we present the neutral stability curve based in the critical overdrive f^* for 16 different heat formations Q with $E^+ = 50$. The solid curve is the calculated f^*. Note that the heat release Q is in logarithmic scale. The smaller dots are the results of Erpenbeck using eigenmode analysis,[13] and the dashed curve is the extrapolated results by Erpenbeck based on the dots. We see a good agreement between our calculated curve and the dots given by his linear analysis.

Two-Dimensional Computational Mesh Setup

In all of the computations presented here, we take the total length of the channel to be $150l^*$ with the detonation front as the right boundary of the computational domain. As the detonation propagates and curves, the interfaces between subdomains will travel at a speed taken to be the averaged speed of the curved detonation front.

In the first subdomain, we use the third order ENO-LF schemes[11] to resolve the reflected shocks and contact discontinuities. The right-hand side of the first subdomain, being the detonation front, will be tracked by the track algorithm in Sec. III. Smoothing III will be applied on the detonation front for every 20 iterations. Chebyshev collocation methods are used in the remaining subdomains.

Effect of Smoothing of the Detonation Front on the Cellular Patterns

To evaluate the effects of smoothing of the detonation front on the cellular structure, we consider the ZND detonation wave with heat formation $Q = 50$, activation energy $E^+ = 50$, and the overdrive $f = 1.6$. The channel width is taken to be $W = 20l^*$. We take a mesh $-\sum_{i=1}^{9}(n, m) = (50, 200) + (24, 50) + (20, 50) + (20, 50) + (20, 40) + (10, 20) + (10, 10) + (10, 10) + (10, 10)$ and $lsk = 160$. The initial size of the subdomains will be $5l^* \times W$, $5l^* \times W$, $5l^* \times W$, $5l^* \times W$, $10l^* \times W$, $15l^* \times W$, $25l^* \times W$, $40l^* \times W$, $40l^* \times W$. Three tests are done to see the effects of smoothing on the cellular pattern.

Test one: smooth I, II, and III. In the first test we activate all three types of smoothing on the detonation front. Thus, strong numerical viscosity will be produced to stabilize the front. In the top part of Fig. 3, we record the pressure on the detonation front for time $t = 30t^* - 40t^*$. A very regular and symmetric two cell structure

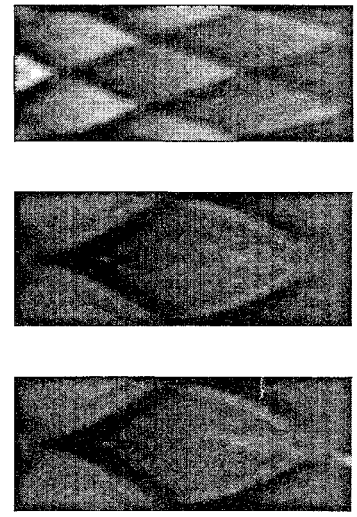

Fig. 3 Cellular patterns: test 1 (top), test 2 (middle), and test 3 (bottom).

is produced by the interaction of four different triple points. This corresponds to a cell width $10l^*$—half the channel width.

Test two: smooth II and III. In the second test, we use smooth II and III, and only one cell is present in the cellular pattern (middle part of Fig. 3) which corresponds to a cell width $20l^*$.

Test three: smooth III only. In the third test, we use only smoothing III. The cellular pattern of the detonation front (bottom part of Fig. 3), also consists of one regular cell almost identical to that of test two.

These tests show us the sensitivity of the cellular patterns of the detonation waves to the amount of numerical viscosity in the scheme. Tests two and three give consistent results that we could use for final calculations. Because of the higher accuracy of the smooth III used in test three, only smooth III will be used in later calculations.

Accuracy of Time Integration and Mesh Convergence Studies

Comparison of time discretizations. We compare the results of the time-splitting method as in Refs. 17 and 18 (which is at most second order) and the third-order Runge–Kutta method with the same resolution and spatial discretizations in the spatial directions. The detonation parameters are $Q = 50$, $E^+ = 50$, $f = 3$; the mesh sizes are $\sum_{i=1}^{9}(n, m) = (120, 150) + (34, 70) + (20, 40) + (20, 40) + (20, 30) + (10, 20) + (10, 10) + (10, 10) + (10, 10)$; and the channel width is $W = 10l^*$. The initial size of the subdomains will be $5l^* \times W$, $5l^* \times W$, $5l^* \times W$, $5l^* \times W$, $10l^* \times W$, $15l^* \times W$, $25l^* \times W$, $40l^* \times W$, and $40l^* \times W$. In Fig. 4, we plot the pressure along the center of the channel at time $T = 34t^*$. The solid line is the results obtained by the third-order Runge–Kutta method, whereas the dash line is the results obtained by the splitting method. We can see that both results agree fairly well except that the splitting method fails to resolve some of the fine structures in the pressure. In the numerical tests given later, the third-order Runge–Kutta method will be used.

Mesh convergence studies. We use the same detonation parameter as before but with three different meshes in the spatial direction. The third-order Runge–Kutta method is used in both cases. Mesh A is $\sum_{i=1}^{9}(n, m) = (100, 100) + (34, 70) + (20, 40) + (20, 40) + (20, 30) + (10, 20) + (10, 10) + (10, 10) + (10, 10)$. Mesh B is $\sum_{i=1}^{9}(n, m) = (120, 150) + (34, 70) + (20, 40) + (20, 40) + (20, 30) + (10, 20) + (10, 10) + (10, 10) + (10, 10)$. Mesh C is $\sum_{i=1}^{9}(n, m) = (160, 200) + (34, 70) + (20, 40) + (20, 40) + (20, 30) + (10, 20) + (10, 10) + (10, 10) + (10, 10)$. The initial size of the subdomains will be $8l^* \times W$, $5l^* \times W$, $5l^* \times W$, $5l^* \times W$, $10l^* \times W$, $12l^* \times W$, $25l^* \times W$, $40l^* \times W$, and $40l^* \times W$. Therefore, in the first subdomain, mesh A is about 10 points per l^*, mesh B is about 15 points per l^*, and mesh C is about 20 points per l^*. In Fig. 5, we plot the temperature and mass fraction of the reactant along the center of the channel. Close agreement can be seen

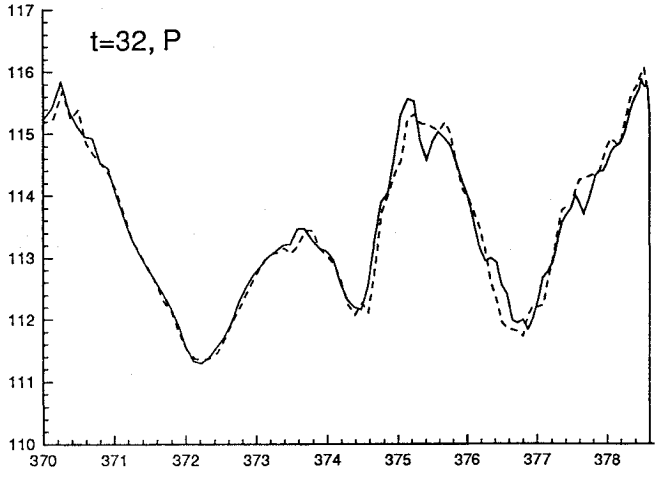

Fig. 4 Pressures along the center of channel obtained by time splitting (dash line) and third-order Runge–Kutta (solid).

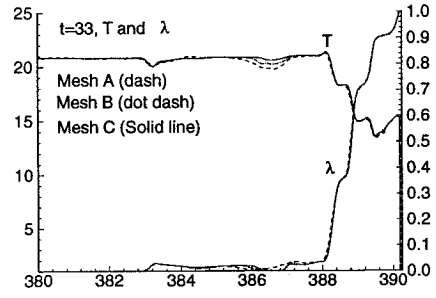

Fig. 5 Temperature and mass fraction of the reactant along the center of channel with three meshes.

among the results for all meshes. In the rest of the computation, we will use at least the resolution of mesh B, which is about 15 points per half-reaction distance. We use this reference mesh even though, during the collision of triple points, the half-reaction distance could be different from that in steady C-J detonation waves.

V. Numerical Simulation of Two-Dimensional Detonation Waves

We present two cases of detonation waves using our high-order hybrid scheme.

Case I: $Q = 10$, $E^+ = 50$, $f = 1.2$, Channel Width $W = 10l^*$, One Cell Pattern

The mesh used in this case is $\sum_{i=1}^{9}(n, m) = (110, 140) + (20, 40) + (20, 40) + (20, 30) + (20, 30) + (10, 20) + (10, 10) + (10, 10) + (10, 10)$ and $lsk = 300$. The initial size of the subdomains will be $5l^* \times W$, $5l^* \times W$, $5l^* \times W$, $5l^* \times W$, $10l^* \times W$, $15l^* \times W$, $25l^* \times W$, $40l^* \times W$, and $40l^* \times W$. This mesh gives a resolution of 14 points per half-reaction distance in the ENO domain. We start the computation with the ZND steady-state solution with a sinelike perturbation (38) on the shock front with $\epsilon = 0.15$.

In Fig. 6, we contour plot five snapshots of the pressure, temperature, vorticity, and mass fraction at time $T = 30.5t^*, 31.5t^*, 32.5t^*, 33.5t^*$, and $34.5t^*$. In Fig. 7, we sketch the interaction of the triple points.

Case II: $Q = 50$, $E^+ = 50$, $f = 1.6$, Channel Width $W = 20l^*$. Two Cells Pattern

We use a mesh $\sum_{i=1}^{9}(n, m) = (50, 250) + (34, 70) + (20, 40) + (20, 30) + (20, 30) + (10, 20) + (10, 10) + (10, 10) + (10, 10)$ and $lsk = 300$. Figure 8 shows a two cell pattern produced by the trajectories of four triple points. There is a larger cell with a width of approximately $10l^*$ (half the channel width) and a smaller one with a width $5l^*$. Figure 9 contains six snapshots of the detonation at time $t = 20.25t^*, 21.5t^*, 22t^*, 22.5t^*, 23t^*$, and $23.5t^*$. The times were chosen so that the interaction of the triple points can be shown clearly in the contour plots. A random perturbation with magnitude $\epsilon = 0.3$ is used to perturb the shock front at $t = 0$. In the first time snapshot $t = 20.25t^*$, in the lower middle part of the channel,

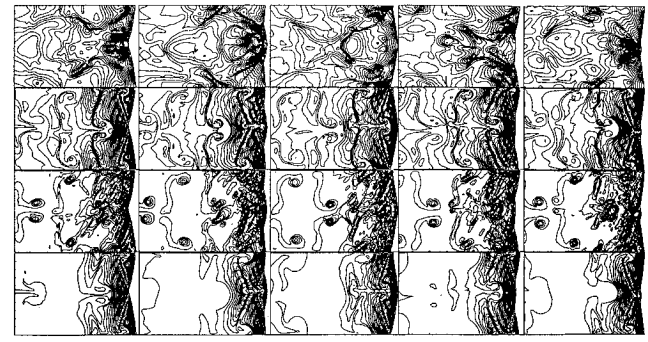

Fig. 6 Case I, $Q = 10$, $E = 50$, $f = 1.2$, and $W = 10$. Five snapshots of pressure, temperature, vorticity, and mass fraction of reactant (from top to bottom) at $t = 30.5t^*, 31.5t^*, 32.5t^*, 33.5t^*$, and $34.5t^*$.

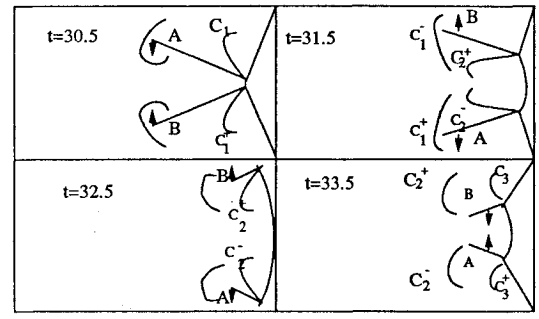

Fig. 7 Case I, $Q = 10$, $E = 50$, $f = 1.2$, and $W = 10$. Sketch of the interaction of the triple points.

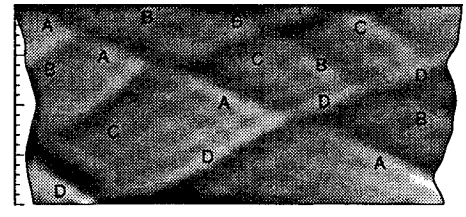

Fig. 8 Case II, $Q = 50$, $E = 50$, $f = 1.6$, and $W = 20$. Tracks of the triple points.

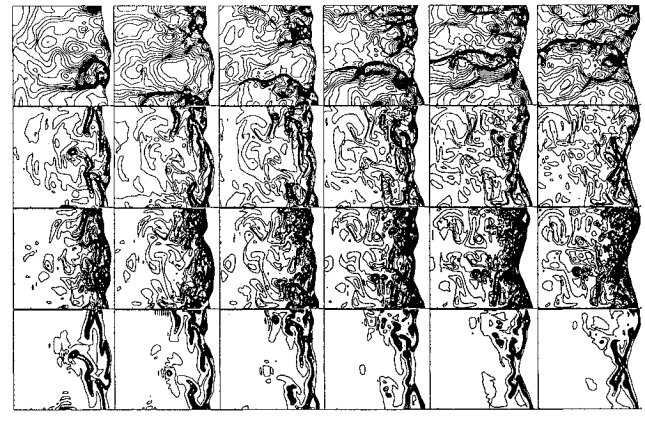

Fig. 9 Case II, $Q = 50$, $E = 50$, $f = 1.6$, and $W = 20$. Six snapshots of pressure, temperature, vorticity, and mass fraction of reactant (from top to bottom) at $t = 20.25t^*, 21.5t^*, 22t^*, 22.5t^*, 23t^*$, and $23.5t^*$.

two triple points C, D are moving away from each other just after collision, and A has been reflected from the upper wall and is about to collide with triple point B. In snapshot 2 ($t = 21.5t^*$), in the upper part of the channel, two smaller triple points A, B collide and separate, and in the middle part of the channel triple point C is moving upward to collide with triple point A. Near the lower wall, triple point D is reflecting away from the lower wall. In snapshot 3 ($t = 22t^*$), triple point B is approaching the upper wall, triple points A and C collide, and triple point D keeps moving up away from

the lower wall. In snapshot 4 ($t = 22.5t^*$), triple point B reflects away from the upper wall and is about to collide with triple point C, whereas triple points A and D are about to collide with each other. In snapshot 5 ($t = 23t^*$), in the upper part of the channel, triple points B and C collide and triple points A and D approach each other. Finally, in snapshot 6 ($t = 23.5t^*$), triple points B and C finish the collision and exchange directions, whereas triple points A and D collide.

Also notice that in snapshots 4 and 5, the two pressure waves from the reflected shocks intersect with each other before the collision of the triple points happens along the detonation front (snapshot 6). Such interaction will cause sudden reaction of any unreacted gas in the interior region and produce so-called "explosions in explosions."

VI. Conclusion

We have developed a high-order numerical scheme that is suitable for computing detailed transverse wave structures of two-dimensional detonation waves. The numerical algorithm uses a multidomain approach so that different numerical techniques can be applied for different components of detonation waves. The propagation of waves across the interfaces of subdomains are smooth, and the order of accuracy of the whole numerical scheme is only limited by the accuracy of the time integrator. Tracking of the detonation front avoids differencing across the detonation front, thus avoiding excessive numerical viscosity as in shock-capturing schemes.

We have shown that the cellular pattern of the detonation waves is affected by the accuracy of the detonation front and the amount of numerical viscosity, especially the amount of viscosity involved in the time evolution of the detonation front by the numerical scheme.

We have studied two cases of detonation waves with specific ratio $\gamma = 1.2$, from small heat release (case I) to large release (case II) and small overdrives (case I) to large overdrives (case II). The numerical results successfully reproduced the onset and evolution of the transverse wave structures. The contact lines within triple points create large vorticity fields behind the detonation front that distort and interact with the detonation front. The contact discontinuities from the triple points after their collisions convect downstream and generate vorticity downstream.

Acknowledgments

This work has been sponsored by a National Science Foundation Grant ASC-9113895 and an Air Office of Scientific Research Grant F49620-94-1-0317 and was partially supported by NASA under Contract NAS1-19480 while the author was in residence at the Institute for Computer Applications in Science and Engineering (ICASE), NASA Langley Research Center, Hampton, Virginia. The computing facility was provided by a supercomputing grant from the North Carolina Supercomputer Center. The author would like to thank Youlan Zhu for his help in developing the shock-tracking algorithms.

References

[1]Urtiew, P. A., and Oppenheim, A. K., "Experimental Observations of the Transition to Detonation in an Exploding Gas," *Proceeding of the Royal Society of London, Series A: Mathematical and Physical Sciences*, Vol. 295, 1966, pp. 13–28.

[2]Berthelot, M., and Vieeille, P., "On the Velocity of Propagation of Explosive Process in Gases," *C. R. Hebd Seances Acad. Sci.*, Vol. 93, 1981, pp. 18–21.

[3]Chapman, W. R., and Wheeler, R. V., "The Propagation of Flames in Mixtures of Methane-Air," *Journal of the Chemistry Society*, Pt. IV, 1926, pp. 2139–2142.

[4]Fickett, W., and Davis, W. C., *Detonation*, Univ. of California Press, Berkeley, CA, 1979.

[5]Strehlow, R. A., *Combustion Fundamentals*, McGraw-Hill, New York, 1984.

[6]Colella, P., Majda, A., and Roytburd, V., "Theoretical and Numerical Structure for Reacting Shock Waves," *SIAM Journal of Scientific and Statistics Computing*, Vol. 4, 1986, pp. 1059–1080.

[7]Engquist, B. E., and Sjogreen, B., "Robust Difference Approximations of Stiff Inviscid Detonation Waves," Univ. of California, Los Angeles, UCLA CAM RT., Los Angeles, CA, 1991, pp. 91–103.

[8]Gottlieb, D., and Orszag, S., *Numerical Analysis of Spectral Methods: Theory and Applications*, SIAM-CBMS, Philadelphia, PA, 1977.

[9]Don, D.-S., Quillen, C., and Shu, C. W., "Supersonic Combustion: Comparative Study Between ENO and Spectral Methods," preprint.

[10]Harten, A., "On High Order Accurate Interpolation for Non-Oscillatory Shock Capturing Schemes," *IMA Program on Continuum Physics and Its Applications*, 1984–85, pp. 72–105.

[11]Shu, C. W., and Osher, S., "Efficient Implementation of Essentially Nonoscillatory Shock Capturing Schemes," *Journal of Computational Physics*, Vol. 77, 1988, pp. 439–471.

[12]Cai, W., Oh, W. H., and Zhu, Y. L., "Direct Numerical Calculations of Neutral Stability Curve of One-Dimensional Detonation Waves," *SIAM Journal of Scientific Computing* (to be published).

[13]Erpenbeck, J., "Stability of Idealized One Reaction Detonations," *The Physics of Fluids*, Vol. 7, 1964, pp. 684–696.

[14]Kopriva, D. A., "Multi-Domain Spectral Solution of Euler Gas-Dynamics Equations," *Journal of Computational Physics*, Vol. 96, 1991, pp. 428–450.

[15]Hyman, J. M., "Numerical Methods for Tracking Interfaces," *Physica*, Vol. 12D, 1984, pp. 396–407.

[16]Taki, S., and Fujiwara, T., "Numerical Analysis of Two Dimensional Nonsteady Detonations," *AIAA Journal*, Vol. 16, 1978, pp. 73–77.

[17]Oran, E. S., Boris, J. P., Flanigan, M., Burks, T., and Picone, M., "Numerical Simulations of Detonations in Hydrogen-Air and Methane-Air Mixtures," *Eighteenth Symposium (International) on Combustion*, The Combustion Inst., 1981, pp. 1641–1649.

[18]Bourlioux, A., and Majda, A. J., "Theoretical and Numerical Structure for Unstable Two-Dimensional Detonations," *Combustion and Flames*, Vol. 90, 1992, pp. 211–229.

[19]Quirk, J. J., "Godunov-Type Schemes Applied to Detonation Flows," NASA CR-191447, ICASE Rept. 93-15, Hampton, VA, April 1993.

[20]Erpenbeck, J., "Nonlinear Theory of Unstable Two-Dimensional Detonation," *The Physics of Fluids*, Vol. 13, 1970, pp. 2007–2026.

[21]Strehlow, R. A., Maurer, R. E., and Rajan, S., "Transverse Waves in Detonations: I. Spacing in the Hydrogen-Oxygen System," *AIAA Journal*, Vol. 7, 1969, pp. 323–328.

[22]Majda, A., "Criteria for Regular Spacing of Reacting Mach Stems," *Proceedings of National Academy of Science*, Vol. 84, 1987, pp. 6011–6014.

[23]Strehlow, R. A., and Engel, C., "Transverse Waves in Detonations: II, Structure and Spacing in H_2—O_2, C_2H_2—O_2, C_2H_4—O_2, and CH_4—O_2 Systems," *AIAA Journal*, Vol. 7, 1969, pp. 492–496.